The Münsterdorf sinkhole cluster:
Void origin and mechanical failure

Georg Kaufmann[1], Douchko Romanov[1], Ulrike Werban[2], and Thomas Vienken[2,3]

[1]Institute of Geological Sciences, Geophysics Section, Freie Universität Berlin, , Malteserstr. 74-100, Haus D, 12249 Berlin, Germany

[2]Department Monitoring- und Erkundungstechnologien, Helmholtz-Zentrum für Umweltforschung - UFZ, Permoserstr. 15, 04318 Leipzig, Germany

[3]Weihenstephan-Triesdorf University of Applied Sciences, TUM Campus Straubing, 94315 Straubing, Germany

Correspondence: Georg Kaufmann (Georg.Kaufmann@fu-berlin.de)

Abstract. Since 2004, collapse sinkholes occur on the sports field of Münsterdorf, a village north of Hamburg in Germany. The sinkholes, around 2-5 m in diameter and 3-5 m deep, develop in peri-glacial sand, which in around 20 m depth is underlain by cretaceous chalk. The chalk has been pushed up close to the surface by a salt diapir. The sinkhole formation initiated suddenly and occurs with a frequency of one every two years.

5   We use a variety of geophysical results (e.g. gravity, electrical resistivity imaging, ground-penetrating radar) from previous field-work campaigns together with a new data set from direct-push based methods to infer mechanical and hydrological properties of the material beneath the sports field (peri-glacial sand, glacial marl, cretaceous chalk).

Based on the derived material properties, we develop a mechanical model for the sinkhole collapse, starting from simple analytical considerations and then moving towards a three-dimensional distinct-element model explaining the sudden onset of
10   collapse sinkholes for the sports field.

The mechanical model supports our hypothesis that the sudden onset of sinkholes is triggered by changes in groundwater level.

1 Introduction

Collapse sinkholes are cylindrical to elliptical surface structures with diameters ranging from one to several hundred meters, and
similar depth extensions (e.g. Waltham et al., 2005; Williams, 2004). Collapse sinkholes form suddenly and pose a substantial
risk to infrastructure because of their sudden inception and almost no warning signs before (e.g. Parise and Gunn, 2007;
De Waele et al., 2011; Kaufmann, 2014; Kaufmann and Romanov, 2016). Often, collapse sinkholes form in karst terrains.

A karst terrain is defined as an area comprising a soluble rock, such as limestone, dolomite, anhydrite, gypsum, or salt.
Common to all this soluble rock types is the ability of water flowing through rock fractures and bedding partings to dissolve
material from the rock walls. While for the first two types of soluble rocks mentioned, limestone and dolomite, dissolution is
substantial only, when the water is acidic, e.g. by dissolving carbon dioxide from air and/or soil to form carbonic acid, for the
latter rock types, anhydrite, gypsum and salt, dissolution occurs in pure water.

The dissolution of soluble rock enhances the initially low primary permeability of the rocks, which is controlled by fractures
in the sub-millimetre range. With time, the developing secondary permeability becomes orders of magnitude larger. The reason
is the enlargement of fissures and bedding partings in the sub-surface, in parts to the meter scale, to form sub-surface voids
and caves. This process occurs naturally over time scales of 10,000-100,000 years (limestone, dolomite), 1,000-10,000 years
(anhydrite and gypsum), and even faster in salt.

Once the sub-surface voids reach a critical size, they can become mechanically unstable and start to collapse. If the void is
deep below the surface, the collapse results in roof and wall breakdown, and breakdown can enlarge the void space by forming
a mechanically stable shape. If the voids develop closer to the surface, breakdown might slowly migrate towards the surface,
until only a thin ledge of rock remains. It is the final collapse of this thin ledge, which causes the sudden appearance of the
collapse sinkhole (e.g. Parise and Lollino, 2011; Lollino et al., 2013).

Depending on the overburden of the soluble rock, collapse sinkholes are classified into pure collapse sinkhole, cover-collapse
sinkhole, and suffosion sinkholes (see Waltham and Fookes, 2003; Waltham et al., 2005; Gutiérrez et al., 2008a, b, and refer-
ences therein).

We discuss a group of collapse sinkholes formed on the sports field in the village of Münsterdorf in northern Germany. These
sinkholes started to appear in 2004 with a rate of one per year, being steep-walled, with a diameter of 2-3 m and 2-5 m deep.
We explore the mechanical stability (or instability) of the locality and try to answer the following questions:

(i) Why do the collapse sinkhole formation starts suddenly in 2004?

(ii) What mechanical conditions are needed to initiate sinkhole collapse?

(iii) Where is the location of the initial sub-surface void responsible for the sinkhole formation?

We have organised the paper as follows: In section 2, we introduce the locality, its geological setup, and we describe the
sinkhole cluster. In section 3, we briefly summarise the results of previous geophysical campaigns, and we derive a lithological
model for the sub-surface structure. We then discuss locations of the initial voids responsible for the sinkhole collapse in terms
of depth and size, and we investigate the chance to spot these voids prior to sinkhole formation with geophysical methods,

depending on their depth. In section 4, we describe several direct push-based methods performed on and around the sports field in Münsterdorf. We then discuss hydrological and mechanical properties derived from these direct push-based methods. In section 5, we first develop a simple mechanical model for sinkhole collapse, and then we apply a discrete-element model to simulate the collapse sinkholes occurring on the sports field. We discuss the mechanical and hydrological properties likely

50 to trigger the collapse sinkholes. In section 6, we come back to our hypothesis of the void origin and present geochemical measurements favouring the deep void origin in the chalk layer. In section 7, we refine our previous hypothesis on the temporal evolution of the collapse sinkholes on the sports field in Münsterdorf. We finally summarise our findings in section 8.

2 Site

The village of Münsterdorf is located around 50 km north of Hamburg in the northern part of Germany (Fig. 1), just south of
the river Stör, which runs in a westerly direction close to Münsterdorf, then turns south to flow into the river Elbe. The river
Stör is the natural local base level for the region, and is influenced by the tides of the North Sea.

2.1 Geological setup

As most of the landscape in Northern Germany, the surface morphology is dominated by the Pleistocene ice-age cycles. The
repeated advance and retreat of the Fennoscandian Ice Sheet carried glacial and peri-glacial sediments, which form the main
features in the landscape: Münsterdorf sits on a geest ridge, a sandy deposits from deposition below the ice, about 20-30 m
above sea level in the region. Beyond this geest island, the landscape is lower, between 5-15 m above sea level, and dominated
by swampy marsh land. The geest ridge has been deposited during the Elsterian (455-320 ka BP) and Saalian (300-125 ka BP)
glacial cycles, while during the last glacial cycle, the Weichselian, the ice did not reach the area around Münsterdorf.

The geest ridge consists of unconsolidated and consolidated peri-glacial sand, interbedded with glacial till, in parts composed
of clay lenses.

The entire region is tectonically controlled by the Krempe-Lägerdorf salt ridge (e.g. Grube, 1955; Köstler and Ehrmann,
1986), a salt diapir, with salt sequences from the Permian Zechstein period. These Zechstein rocks can usually be found in a
depth range between 3-5 km underneath northern Germany, but as the salt layers in the Zechstein evaporites can flow plastically
under stress, numerous salt structures have been pushed up by the large stress imposed by the overburden. The vertical uplift
of these salt domes has pushed up the overburden by several kilometres, often reaching the surface. In the Münsterdorf region,
the Krempe-Lägerdorf salt ridge has pushed up cretaceous chalk from its original depth of 0.5-1 km to a position close to the
surface (e.g. Grube et al., 2017; Grube and Rickert, 2019).

Just 1.5 km south-west of Münsterdorf, the chalk is just below the surface (6 m below ground), and several large open-pit
mines exploit the material. The deepest open-pit mine reaches down to 90 m below sea level, which requires a substantial effort
to dewater the mines (e.g. Iwanoff, 1998). The pumped groundwater from the open-pit mines is routed via an artificial channel
in the east towards the river Stör. In the mines, numerous karst features can be observed, such as dissolutionally-enlarged
fissures and bedding planes and small collapse sinkholes.

On the southern rim of the village of Münsterdorf, the local sports field is located. The chalk can be found here in around
20 m depth below the sports field (see Fig. 1), confirmed by several boreholes (see Kirsch and Werner, 2008; Kirsch et al.,
2011; Göthling et al., 2010, and references therein). Above the cretaceous chalk, we find mainly peri-glacial sand, inter-bedded
with glacial till.

From the geological and morphological setup, we identify three key aspects responsible for the presence of karst structures
in the Münsterdorf region:

- Salt diapirism responsible for local tectonics and uplift of Permian and Cretaceous sequences,

- thus cretaceous chalk in around 20 m below sports field,

- and landscape morphology dominated by ice-age cycles, with deposition of glacial till as flow barrier.

The glacial till with its lower hydraulic permeability confines groundwater flow, the salt diapirism caused chalk layers to the uplifted close to the surface (see also Kaufmann et al., 2018).

2.2 Sinkhole cluster

90 Since 2004, collapse sinkholes occur regularly on the sports field (Fig. 2). These collapse sinkholes are about 2-3 m in diameter and about 3-5 m deep, exposing the peri-glacial sand. No groundwater can be found in the sinkholes, as the groundwater table nowadays is lower. The sinkholes are aligned along a narrow band about 50-70 m wide and 300 m long, striking in west-easterly direction.

The sudden onset of the sinkhole occurrence and the limitation to the narrow band suggests a relation to a lithological feature
95 in the sub-surface, and a possible inception by a change in hydraulic conditions (e.g. Kaufmann et al., 2018). Thus, we regard these two aspects as important constraints for the explanation of the collapse sinkholes along the sports field in Münsterdorf: (i) Sudden onset in around 2004, (ii) Restriction to narrow west-east band.

3 Geophysical site exploration

Since the sudden onset of sinkholes on and around the sports field in 2004, several geophysical investigations have been carried
100   out (e.g. Kirsch, 2009; Gebregziabher-Gared, 2010; Harland, 2010; Kirsch et al., 2011; Schulze-Dieckhoff, 2015; Timm, 2015; Tippelt et al., 2017; Mai et al., 2017; Kaufmann et al., 2018), with the aim to (i) find the cause of the sinkholes, (ii) characterise the sub-surface beneath the sports field.

3.1 Previous work

From the numerous geophysical methods used (gravity, geoelectrics, electro-magnetics, georadar, seismics, borehole-based
105   spectrally-induced polarisation), especially geoelectrics and georadar have been successful to delineate the glacial till from the peri-glacial sand. In almost all profiles (taken in north-south direction), the high-resistivity peri-glacial sand is thin (1-2 m) in the north and underlain by more conductive glacial till, while the peri-glacial sand becomes thicker (5-8 m) towards the south, while the glacial till seem to be thinner and more isolated in the south. These results can be explained by the geest island, on which Münsterdorf rests, which peters out towards the south (Fig. 3). Cored boreholes confirm this setup locally
110   (e.g. Kaufmann et al., 2018).

The chalk layer in about 20 m depth has not been identified in the geoelectric and georadar measurements, because electrical conductivities between the chalk and wet till are too similar for the former method, and because of depth restrictions for the latter method. However, in seismic p-wave profiles, the chalk layer can be seen.

From the geophysical and borehole measurements, we have derived a simplified lithological setup underneath the sports
115   field:

- Three layers, peri-glacial sand, glacial till, soluble chalk.

- Peri-glacial sand varies from 2 to 8 m thickness, becoming thicker in the south.

- glacial till massive in the north (several meter thick), and peters out towards the south.

- Chalk in an almost constant depth of 20 m below surface underneath the sports field.

120   We will discuss this simplified setup in more detail later, with more sub-divisions of glacial sand and till, based on our results of the direct push-based methods.

We argue that the soluble chalk in shallow depth is accessible to ground water and thus has the potential to be dissolved, resulting in karstified structures. However, as stated below in our first hypothesis, there is also the possibility that voids are present in the sand layers.

125   ### 3.2 Hypothesis

To start our discussion on the origin of the sub-surface voids, we propose two different competing scenarios for the development of the collapse sinkholes:

1. **Non-karstified:** The initial void causing the sinkhole collapse has developed above the lower till layer, in about 6-8 m depth in the peri-glacial sand.

As we know the sinkhole sizes ($w = 2 - 3$ m diameter, $d = 2 - 5$ m depth), the initial void should have a volume around $V = \pi \frac{w}{2}^2 d \in [6, 35]$ m^3, a substantial initial void, which in this depth should possibly be detectable by geophysical methods. We will try to estimate the effect on gravity and ERT surveys below.

We note that in this scenario the initial void would be located in insoluble unconsolidated rocks, thus the origin of the void cannot be dissolution of material, only either removal of material by erosion of melting of a block of ice. We then have to ask us, why such a void is only present along the narrow band on the sports ground, and not much more widespread, as expected in a landscape dominated by glacial features.

2. **Karstified:** The initial void causing the sinkholes developed in the chalk in around 20 m depth by chemical dissolution of the rock. The initial void volume must be similar as above.

In Kaufmann et al. (2018) we have argued that initial voids can have developed in the top part of the chalk, because surface water undersaturated with respect to calcium is diverted into deeper zones. The reason for surface water to reach the chalk layer is the lower hydraulic conductivity of the glacial till, which is more prominent underneath the northern part of the sports field. This massive glacial till in the northern section of the sports field acts as a flow barrier, forcing surface water to greater depths. Here, the aggressive water with calcium concentrations below the calcium-equilibrium concentration creates (on time scales of 10,000-100,000 years) dissolutionally-enlarged voids, having meter-size dimensions. The voids are mechanically meta-stable, because the water in the voids with its buoyancy counteracts gravity (which we show later by modelling).

In this case we speculate that the over-consolidated lower peri-glacial sand layer, which is directly above the initial void, has been loosened and then slowly drops into the karst void, but the layers above the peri-glacial sand were kept in place by the finite strength of one of these layers. Thus the initial void started migrating upwards, into the saturated zone. A drop of the groundwater table through mining (as discussed in Kaufmann et al., 2018) then removed the buoyant support for the overburden, and the upper layers finally collapse.

3.3 Geophysical forward modelling

In our summary on the geophysical work done over the years, we mentioned the identification of the lithological setup of the region around the sports field. However, geophysical exploration was less successful in identifying the sub-surface voids causing the collapse sinkholes. Only old sinkholes show a faint signal in georadar and (in parts) in geoelectrical measurements.

We therefore present results from forward modelling of gravity and geoelectrical signals induced by sub-surface voids in a simplified setup (Figs. 4 and 5): A top layer of dry peri-glacial sand (0-10 m), followed by a wet layer of peri-glacial sand (10-20 m), and below the soluble chalk (>20 m). Depending on the hypothesis, voids are either (i) in the peri-glacial sand (air-filled, see Fig. 4), or (ii) in the chalk (water-filled, see Fig. 5). Material properties are listed in table 1.

160   The gravity forward model is based on box models for the lithological layers, and spheres for the voids (e.g. Blakely et al., 2010). All density values are referenced against the chalk density, thus the calculated Bouguer gravity values will be negative, as peri-glacial sand and voids have lower densities, when compared to the chalk.

For the electrical resistivity model, we first create a 2D forward model with *res2Dmod* (e.g. Loke, 2016) to calculate apparent resistivities for the given setup, and these apparent resistivities can than be loaded into *res2Dinv* (e.g. Loke and Barker,
165   1995, 1996) to find the resulting resistivity model from inverse modelling. The forward model assigned is perturbed a a random error of up to 2% of the resulting apparent resistivities.

Following our two hypotheses for the void origin, the *non-karstified* and the *karstified* case, we define two forward models with voids in different depths: (i) Shallow origin (6-8 m) in insoluble dry sand, air-filled voids, (ii) deeper origin (20-22 m) in soluble chalk, water-filled voids. We locate three voids in these two different depth ranges, with increasing radius from left to
170   right (1.1, 1.7, and 2.0 m) to account for the uncertainty in initial void volume introduced before.

– **Non-karstified:** In the non-karstified setup (Fig. 4), the voids are located in the dry peri-glacial sand. The Bouguer gravity is negative, because the density of the peri-glacial sand (1800-19000 kg/m^3) is lower than the density of the chalk (2600 kg/m^3), which we took as reference density. The air-filled voids are modelled with a density of 0 kg/m^3. All three initial voids are visible in the Bouguer signal, but the amplitude (less than 1 mGal) would be hard to detect within
175   the accuracy of a typical relative gravimeter.

In the ERT cross section, we used electrical resistivities of 1000 Ωm for the dry peri-glacial sand, and 800 Ωm for the air-filled voids. Below, both the wet peri-glacial sand and the chalk are more conductive, with values around 200 Ωm. The resulting resistivity model can distinguish between dry sand and wet sand/chalk, but does not reveal the void spaces, as there resistivity is too close to the one of the dry sand.

180   – **Karstified:** In the karstified setup (Fig. 5), we moved the voids down to the top of the chalk, with a water-filled void density of 1000 kg/m^3 and a void resistivity of 0.5 Ωm, resembling water with dissolved ions. The Bouguer gravity signal now is rather uniform, reflecting the mass deficit of the peri-glacial sand, but no clear indication of the voids. In the ERT cross section, resistivities again identify the interface between dry and wet sand, but the low-resistivity voids within the low-resistivity chalk cannot be seen.

185   From this simple forward modelling exercise, we would expect to find hints for initial voids from geophysical signals (mainly gravity), if these initial voids would be in the shallow peri-glacial sand. For a deeper-seated origin of the voids, e.g. in the chalk, no clear geophysical signal both in gravity and geoelectrics can be expected. As outlined in Kaufmann et al. (2018), we have not found evidence for sub-surface voids in the geophysical data.

4 Direct push-based methods

In this section, we discuss results from direct push-based methods applied to several locations on the sports field, which we use to characterise the hydrogeological regime and relevant mechanical parameter values for the the site. The results from the direct push-based methods provide high-resolution data for geomechanical and hydrogeological properties of the sub-surface.

This new field data will complement the existing geophysical data set used to derive a lithological model for the Münsterdorf sports field and its vicinity. For the numerical modelling discussed later, the results from the direct push-based methods are mandatory to calibrate the models.

The area around the sports field has been probed extensively by several direct push-based methods (e.g. Vienken et al., 2012). These versatile in-situ measurements can be used in unconsolidated and weakly consolidated sediments to obtain vertical high-resolution profiles of a number of material properties, e.g. mechanical failure criteria, hydraulic parameter values, and electrical conductivities, as we will outline below. From the measured parameter values listed above, several hydrological and mechanical material properties can be derived:

(i) HPT (Hydraulic profiling tool): Water is injected with a flow rate Q [m³/s] from the direct push-based probe into the surrounding unconsolidated rock, the back pressure p [Pa] is measured and used to delineate hydro-stratigraphic units within the subsurface. The ratio of flow rate and back pressure (corrected for air pressure and hydro-stratigraphic pressure) can be used as proxy that can be correlated to hydraulic conductivity, K [m/s], of the material probed (e.g. Rogiers et al., 2014).

Relative HPT hydraulic conductivity, referring to the ratio of HPT injection rate Q and back pressure P, can be correlated with hydraulic conductivity ΔK_h [m/s] (e.g. McCall, 2011):

$$\Delta K_h = 21.14 \ln \left(\frac{Q}{P} \right) - 41.71, \tag{1}$$

Note that Q is in ml and P in psi in this ratio.

(ii) EC (Electrical conductivity): By injecting an electric current I [A] from the probe into the ground and measuring the resulting electrical potential U [V], electrical conductivity σ_e [Sm] can be calculated (e.g. Christy et al., 1994).

(iii) CPT (Cone penetration testing): A cone can be pushed at constant speed into the ground, and the force at the tip of the cone can be measured and normalised to the cone surface area to obtain the cone pressure q_c [Pa]. Additionally, the force acting along the side of the cone can be measured, and normalised by the so-called sleeve area to obtain the sleeve friction f_s [Pa] (Lunne et al., 1997).

To estimate the failure of the material under stress, both the friction angle α_f and the shear strength μ_0 can be derived. The friction angle is related to the cone pressure q_c (DIN Deutsches Institut für Normung e.V., 2011):

$$\alpha_f = f(q_c), \tag{2}$$

with the function f tabulated in geotechnical manuals (e.g. DIN Deutsches Institut für Normung e.V., 2011).

220   The undrained shear strength u_c [Pa] can be calculated from the cone pressure q_c and the overburden stress q_{v0} [Pa] as (Lunne et al., 1997):

$$u_c = \frac{q_c - q_{v0}}{N_k},$$
(3)

with N_k an empirical cone factor, around $N_k \sim 17$ for over-consolidated clays (e.g. Kjekstad et al., 1978), and $N_k \sim 11-$

19 for normally-consolidated marine clays (e.g. Lunne and Kleven, 1981). The overburden stress can be approximated

225   as $q_{v0} = \rho g h$, with ρ [kg/m^3] the average density, g [m/s^2] gravitational acceleration, and h [m] the thickness of the overburden.

With the two quantities friction angle and undrained shear strength, the shear stress σ_s [Pa] as a function of normal stress σ_n [Pa] can be defined as:

$$\sigma_s = \mu_0 + \sigma_n \tan(\alpha_f),$$
(4)

230   which can be used to evaluate the likelihood that the material will break under certain applied stresses. Here, we assume $\mu_0 \simeq u_c$.

From cone pressure q_c and sleeve friction f_s, the soil-behaviour type (SBT) index can be calculated, following Robertson (2016):

$$SBT = \sqrt{\left[3.47 - \log\left(\frac{q_c}{p_a}\right)\right]^2 + [\log R_f + 1.22]^2}$$
(5)

235   with our cone pressure q_c defined earlier, p_a [Pa] the atmospheric pressure, $R_f = \frac{f_s}{q_c}$ the friction ratio, and f_s [Pa] the sleeve friction defined earlier. The SBT index characterises soil types, as is maps the q_c-f_s parameter space, and thus the position in the Mohr circle.

(iv) SMP (Soil moisture probe): Electrical permittivity ϵ_r [-] can be measured in the frequency domain to derive the soil moisture content Θ [-], which for the saturated zone is equal to the porosity Φ [-] (e.g. Vienken et al., 2013).

240   From the dielectric permittivity ϵ_r measured, we can derive the volumetric water content Θ [-] from an empirically fitted relation (e.g. Topp et al., 1980):

$$
\begin{aligned}
\theta &= -5.3 \times 10^{-2} + 2.92 \times 10^2 \epsilon_r \\
&- 5.50 \times 10^4 \epsilon_r^2 + 4.3 \times 10^{-6} \epsilon_r^3
\end{aligned}
$$
(6)

In the saturated zone, the volumetric water content is equal to the porosity Φ [-]: $\Theta = \Phi$.

All direct push-based methods listed above have been carried out along a south-north transect on the western edge of the

245   sports field, thus the locations are aligned perpendicular to the sinkhole zone (for locations see Fig. 2).

The following lithological units can be identified from the combined interpretation of the direct push-based methods (Fig. 6):

(i) Well-sorted sand and silty sand (peri-glacial sand), (ii) poorly-sorted sand/till layers (glacial till), (iii) dissolved chalk along

the maximum depth reached by the direct-push measurements. Thus, the direct-push inferred setup provides more details, when compared to the simpler lithological structure derived earlier from other geophysical methods: The glacial till can be further

250 sub-divided into an upper discontinuous layer (3-5 m depth), and a lower more continuous till layer (10-12 m depth). The lower till layer can be characterised as aquitard based on the results from the HPT measurements.

It is interesting to note that the direct push-based profile performed at investigation point 5 (see Fig. 6) reveals an isolated depth interval of increased relative hydraulic conductivity within the chalk. This isolated interval is also characterised by increased values of measured electrical conductivity. The combination of these two elevated parameter values can be interpreted

255 as karstified zone: Having a high hydraulic conductivity, and water enriched with dissolved species from the chalk, e.g. calcium and bicarbonate. This is also supported by a CPT log that was performed through an artificially filled sinkhole in approximately 10 m distance to the HPT probing location 5. This CPT log, which was in contrast to the other CPT measurements able to reach into the chalk layer, shows an area with very low cone resistance (indicating very weak and/or loose material) between 22-27 m below ground surface.

260 Mechanical properties have been estimated from the CPT measurements (see also tab. 1). While the glacial till seems to have a friction angle around $\alpha_f \simeq 37°$ and an undrained shear strength around $u_c \simeq 70 - 150$ Pa, the peri-glacial sand is stronger, with a friction angle around $\alpha_f \simeq 40 - 42°$ and an undrained shear strength of $u_c \simeq 300$ Pa in the upper part and up to $u_c \simeq 500 - 600$ Pa in the lower part of the cross section. It seems that the lower package of peri-glacial sand is over-consolidated, a result from the high normal stress induced during the ice-covered phases (Elsterian and Saalian). The peri-glacial sand above

265 the lower till layer is also strong, except in the zone, where the sinkholes occur (friction angles around $\alpha_f \simeq 35°$).

From the results of the direct push-based methods, with the almost continuous lower till layer being (at least in parts) an aquitard, we continue discussing mechanical models for the sinkhole collapse to elucidate, which of our two hypotheses is more likely.

5 Mechanical models

270 In this section, we introduce and discuss mechanical concepts and models, which we will use to describe the sudden occurrence of collapse sinkholes on the sports field. We start with simple analytical stability considerations, which serve as base for more complicated discrete-element mechanical deformation models.

5.1 Simple mechanical models

We first discuss two simple end members of a situation prone to collapse sinkhole generation (e.g. Panno et al., 2013;
275 Messerklinger, 2014), a first case considering buoyancy only, and a second case assuming that part of the stresses are supported by a stronger elastic material.

5.1.1 Buoyancy driven model

We define a two-layer setup (Fig. 7 top), with consolidated sediments of thickness H [m] on top and a density of ρ_s [kg/m^3], underlain by soluble rock of density ρ_c. Below the depth H, a circular void of radius a [m] is present, created by dissolution
280 of the rock. The void is either water-filled, with the density of water $\rho_w \simeq 1000$ kg/m^3, or air-filled, with a density of $\rho_a \simeq 0$. Thus, in this setup, a vertical cylinder (thin dashed line) with cross section $A = \pi a^2$ [m^2] and volume $V = \pi a^2 H$ [m^3] hangs above the void, and is kept in place by buoyancy and friction along its side walls.

We then can derive a force balance:

$$\boldsymbol{F}_G - \boldsymbol{F}_B - \boldsymbol{F}_R = 0, \tag{7}$$

285 with $\boldsymbol{F}_G$ and $\boldsymbol{F}_B$ [N] the gravitational and the buoyancy forces, acting in the normal direction, and $\boldsymbol{F}_R$ the frictional force, acting on the side of the column. Considering only the vertical component of the force balance (e.g. $\boldsymbol{F}_G = (0,0,F_G)^T$), and solving for the frictional force, we obtain:

$$F_R = F_G - F_B = \rho_s g V - \rho_{w/a} g V = (\rho_s - \rho_{w/a}) g \pi a^2 H. \tag{8}$$

Note that the variable $\rho_{w/a}$ means either water or air density. Rewriting (8) to a shear stress by using $\tau_R = \frac{F_R}{A_R}$ [Pa], with
290 $A_R = 2\pi a H$ the side hull of the cylinder, we obtain:

$$\tau_R = \frac{(\rho_s - \rho_{w/a}) g a}{2}. \tag{9}$$

We now define a standard model with parameter values similar to the Münsterdorf sinkholes: Sinkhole radius $a = 1.5$ m, depth of unconsolidated rock column above void $H = 20$ m, and gravitational acceleration $g = 9.81$ m/s^2. For a sediment density of $\rho_s \simeq 2000$ kg/m^3, a water density of $\rho_w = 1000$ kg/m^3, and air density of $\rho_a = 0$, as shear stress we find for a
295 water-filled and an air-filled void, respectively:

$$\tau_R(\text{water-filled}) \quad \sim \quad 7.4 \text{ kPa,}$$
$$\tau_R(\text{air-filled}) \quad \sim \quad 15 \text{ kPa.}$$

This result exemplifies the minimum shear stress needed to support the hanging column in both cases, water-filled and air-filled cavity. If the measured shear stress is above the maximum value of 15 kPa, the hanging column remains stable, the void is kept

300 open. For shear stresses below this threshold, the column drops into the void and a collapse sinkhole forms.

5.1.2 Flexure- and buoyancy-driven model

For the second example (Fig. 7 bottom), we consider the same setup as above, but this time the vertical cylinder is hold in place by a thin ($2h$) elastic layer. From the force balance, we can derive the classical equation for a thin elastic plate under surface loading q (e.g. Turcotte and Schubert, 1982) with isotropic and homogeneous material properties:

305 $$D\nabla^4 w = -q, \tag{10}$$

with D [Nm] the flexural rigidity, w [m] the vertical deformation, and q [Pa] the load acting on the plate (in vertical direction). For the flexural rigidity, we use (e.g. Turcotte and Schubert, 1982):

$$D = \frac{(2h)^3 E}{12(1-\nu^2)}, \tag{11}$$

with E [Pa] the Young modulus, ν [-] the Poisson ratio, and $2h$ [m] the plate thickness. Considering a thin circular plate

310 of radius a [m], which is fixed around its perimeter, an analytical solution of (10) can be derived within the framework of Love-Kirchhoff plate theory: (e.g. Reddy, 2007):

$$w(r) = -\frac{q}{64D}\left(a^2 - r^2\right)^2. \tag{12}$$

Defining the load as the sum of the vertical sediment cylinder $\rho_s gH$, the buoyancy induced by the water-filled void $\rho_w gH$, and assuming wall friction, τ_R along the side of the column we arrive at:

315 $$\begin{aligned} q_{full-load} &= \rho_s gH - \rho_{w/a} gH - \tau_R \\ &= (\rho_s - \rho_{w/a})gH - \tau_R. \end{aligned} \tag{13}$$

Inserting (13) into (12), we now can calculate the deflection of the supporting layer in the center ($r = 0$). For a Young modulus of $E \simeq 10$ GPa, a Poisson ration of $\nu \simeq 0.3$, and a plate thickness of $2h = 0.6$ m, the deflection for a water-filled resp. an air-filled void is:

320
$$\begin{aligned} w(\text{water-filled}) &\sim 0.08 \,/\, 0.06 \text{ m}, \\ w(\text{air-filled}) &\sim 0.16 \,/\, 0.14 \text{ m}, \end{aligned}$$

with the left values assuming no wall friction ($\tau_R = 0$), the right value assuming a wall friction of $\tau_R = 50$ kPa (a higher value than the minimum shear stress derived before).

However, the more important parameter is the thickness of the elastic layer h as, according to (11), it scales with the power of three.

We now want to estimate, when the elastic layer will break. We therefore need to calculate the stresses in the thin elastic plate:

$$
\begin{aligned}
\sigma_{rr} &= -\frac{3qz}{32h^3}\left[(1+\nu)a^2 - (3+\nu)r^2\right], \\
\sigma_{\theta\theta} &= -\frac{3qz}{32h^3}\left[(1+\nu)a^2 - (1+3\nu)r^2\right], \\
\tau_{r\theta} &= 0,
\end{aligned}
\tag{14}
$$

with z [m] the vertical coordinate, $z \in [-h, h]$. As the shear stress $\tau_{r\theta}$ is zero, the two normal stress σ_{rr} and $\sigma_{\theta\theta}$ are the two principal stresses, which we term $\sigma_1 = \sigma_{rr}$ and $\sigma_2 = \sigma_{\theta\theta}$. The maximum values for these two normal stresses are obtained for $r = a$ and $z = h$:

$$
\begin{aligned}
\sigma_{rr}^{max} &= +\frac{3qa^2}{16h^2}, \\
\sigma_{\theta\theta}^{max} &= +\frac{3qa^2}{16h^2}\nu.
\end{aligned}
\tag{15}
$$

Using the material parameter values from our numerical example above, the normal stresses are:

$$
\begin{aligned}
\sigma_{rr}^{max}(\text{water-filled}) &\sim 920 \text{ kPa}, \\
\sigma_{\theta\theta}^{max}(\text{water-filled}) &\sim 276 \text{ kPa}, \\
\sigma_{rr}^{max}(\text{air-filled}) &\sim 1839 \text{ kPa}, \\
\sigma_{\theta\theta}^{max}(\text{air-filled}) &\sim 552 \text{ kPa}
\end{aligned}
$$

Note that reducing the plate thickness to 50% increases both normal stresses by a factor of 4!

For the two principal stresses, we can calculate the center M_c and the radius M_r of the Mohr circle as (e.g. Stüwe, 2013):

$$
\begin{aligned}
M_c &= \frac{\sigma_1 + \sigma_2}{2} = 598/1196 \text{ kPa}, \\
M_r &= \frac{\sigma_1 - \sigma_2}{2} = 322/644 \text{ kPa},
\end{aligned}
\tag{16}
$$

with the values given for a water-filled and an air-filled void, respectively.

The two Mohr circles are shown in Fig. 8, along with the lines of failure for the glacial till and the peri-glacial sand. For the failure lines, parameter values have been taken from the results of the direct push-based methods discussed before. If the column above the void is supported by the buoyancy of water, the Mohr circle is below the line of failure. Removing the buoyant support moves the Mohr circle closer to the failure line. Here both the thickness of the elastic plate, $2h$, and the Poisson ratio, ν, strongly control the failure: Reducing either one or both of these values results in a Mohr circle crossing the failure line.

Thus we have shown with our simple analytical examples that a collapse sinkhole with size and depth typical to the Münsterdorf sinkholes can form, if the buoyant support of the material above the void is reduced.

Next, we extend our simple setup to a three-dimensional mechanical model, based on the discrete-element method.

5.2 Discrete-element mechanical models

The discrete-element method (DEM) is a computational method to simulate the interaction of a large number of particles (e.g. Cundall and Strack, 1979). Often, the particles are spheres with pre-described radius and some material properties such

350   as density ρ [kg/m^3], Young modulus E [Pa], and Poisson ratio ν [-]. Spheres are packed into a three-dimensional region to represent a macroscopic material, with packing being either regular or irregular. Neighbouring spheres can interact, with a large choice of mechanical laws defined. Modelling of the mechanical deformation consists of several steps: (i) setup of modelling domain, (ii) packing with spheres, (iii) definition of material properties and interaction laws, (iv) time-stepping procedure to track position and velocity of each sphere.

355   We use the open-source DEM model YADE (e.g. Scholtés and Donzè, 2012, 2013; Šmilauer et al., 2020). Our modelling domain is 50×50×50 m in size, thus ten times larger than the collapse sinkholes in Münsterdorf (Fig. 9). This large modelling domain ensures that the fixed boundary spheres (also shown in red as the chalk) have no influence on the deformation (see Romanov et al., 2019, for more details on the implementation). The material properties for the different layers (upper and lower peri-glacial sand, glacial till, chalk) have been taken from the literature (Young modulus, Poisson ratio) and from the direct
360   push-based methods discussed above (friction angle and cohesion).

The spheres in the initial model (upper and lower peri-glacial sand: light brown; glacial till: orange; chalk: red) are packed, and the model is stable, thus no deformation is observed (Fig. 10 top). We then initiate a void in the chalk (red spheres) by removing spheres within a given radius (removed spheres marked in blue). The removed spheres represent either a water- or an air-filled initial void. This initial void in the chalk destabilises the model domain mechanically. The material above the void
365   starts to break down into the void, until a new mechanical equilibrium is reached.

Two scenarios are shown in Fig. 10 (middle and bottom row).

(i)   **Buoyant support:** In the left column, the sub-surface is characterised by a high water table, the initial void is filled with water. Thus the difference between gravitational force and buoyancy force is smaller, $(\rho_s - \rho_w)g$, and thus the buoyant force compensates the gravitational force significantly. The model experiences breakdown of sand layers above
370   the chalk, but the elastic strength of the till supports the weight of the column above and the void does not migrate towards the surface. The initial void enlarged by chemical dissolution becomes enlarged by additional breakdown, but remains stable. No collapse sinkhole will form (unless the boundary conditions are changed).

(ii) **No buoyant support:** In the right column, we reduce the buoyant force, the initial void is air-filled, simulating a drop in water table, as possibly initiated by groundwater withdrawal. The difference between gravitational force and buoyancy
375   force becomes larger, $(\rho_s - \rho_a)g$ with $\rho_a \simeq 0$, and thus the overlying column experiences a stronger downward force. In this model, the initial void also enlarges through roof collapse, but the overlying layers cannot support the weight any more, the entire overburden slips into the void and a collapse sinkhole appears suddenly on the surface.

By comparing these two models we have shown, that a simple change in the hydraulic boundary condition, here a drop in water table, which reduces buoyancy and thus increases the weight of the column hanging above the void, can trigger a collapse
380   sinkhole.

We stress that the time scales of dissolution and mechanical breakdown are completely decoupled: While the void in the chalk, created by chemical dissolution of the material on time scales of $1,000 - 100,000$ years, might initiate roof collapse into the insoluble formation, the surface remains stable, because the overlying material is partially supported by the mechanical

strength of the layers. However, a drop in water table through groundwater withdrawal on time scales of years can destabilise

385 the system, and initiate a sudden collapse of the surface, creating a collapse sinkhole.

Of course one can argue that a similar situation might occur for a void located in the peri-glacial sand. However, we have no evidence for a mechanically sound layer in the top part of the insoluble overburden (down to 6-8 m), thus a potential sub-surface void in the peri-glacial sand is unlikely to be mechanically meta-stable, but will collapse more or less immediately. Thus we argue that the void origin is more likely to be in the chalk layer. We will support this argument further in the next

390 section.

6 Chemical considerations

In this section, we pick up the *short-term* mechanical failure models developed in the last section in view of the *long-term* evolution of the sinkhole cluster on the sports field. With the mechanical models presented before we have shown, that a water-table drop can trigger the sinkhole collapse. The initial void, however, can be present in the sub-surface for a long period before
395   the collapse.

We want to continue the discussion on the origin of the voids in the surface. In section 4, we have discussed the lower glacial till layer, which seems to be a continuous structure in around 12-15 m depth, with possible interruptions in the sinkhole zone. Hints for these interruptions come from the higher hydraulic conductivities and the elevated electrical conductivities in boreholes crossing the sinkhole zone, which might indicate water from the chalk, enriched with dissolved matter (we come
400   back to this argument later).

6.1 Chemistry

From the direct push-based electrical conductivity measurements, we found values for the electrical conductivity around $\sigma_{e,f} \simeq$ $30 - 50$ mS/m where direct-push profiling reached the hydraulically conductive part of the chalk, in parts even higher. We convert this electrical conductivity representative for the fluid, $\sigma_{e,f}$ [μS/cm], to the total amount of dissolved solids, TDS
405   [mg/l], using an experimentally determined linear relation (e.g. Lloyd, 1985; Atekwana et al., 2004)

$$TDS = k_e \sigma_{e,f}, \tag{17}$$

with $k_e \in [0.55, 0.80]$ [cm mg / l / μS] a correlation factor, and the electrical conductivity $\sigma_{e,f}$ [μS/cm] in this equation referenced to 25°C. Using $k_e = 0.6$, we obtain a TDS value around 180-300 mg/l.

When we argue that a large amount of the TDS value can be explained with dissolution of the chalk, we derive the concen-
410   tration of calcium c [mol/m^3] from the TDS value, using

$$c = \frac{TDS}{m_r}, \tag{18}$$

with $m_r = 0.101$ kg/mol the atomic mass of calcite, resulting in $c \sim 2 - 3$ mol/m^3.

If we compare this calcium concentration c derived from TDS to the calcium equilibrium concentration c_{eq} [mol/m^3] for calcite dissolved under closed-system conditions (decoupled from the atmosphere), which is in the range of $c_{eq} \simeq 2 - 5$ mol/m^3
415   (e.g. Buhmann and Dreybrodt, 1985a, b), we find that the dissolution of chalk is close or at its equilibrium value, thus at its maximum.

Arguing that the high calcium concentration in the probed water in the chalk has been attained locally, the EC results from direct push-based methods support the idea of Kaufmann et al. (2018), that enlargement of voids in chalk by chemical dissolution has created the initial void space in around 20 m depth. The isolated area of high permeability within the chalk,
420   that was identified using the direct push-based HPT as well as the depth interval with strongly reduced cone pressure (CPT measurement), support the theory that the high calcium concentration has been generated by the local dissolution, creating a large secondary permeability in the chalk.

7 Interpretation

In Kaufmann et al. (2018), we have developed a simple hypothetical model for the formation of sinkholes on the sports
425 field in Münsterdorf. With the additional information gained in this work from the direct push-based methods, the short-term
mechanical collapse models, and estimates of the chemical composition of the groundwater, we are now able to refine our
previous hypothesis.

The cross sections in Fig. 11 follow a temporal evolution (from top left via bottom towards top right). Shown are three
lithological units, chalk (light blue), peri-glacial sand (yellow), and glacial till (brown). The thick blue line depicts the water
430 table.

From our evolution models, we speculate that groundwater is forced to flow vertically down in the middle of the section,
because the glacial till present in the northern part is less hydraulically conductive. The groundwater, undersaturated with
respect to calcium, reaches the chalk in around 20 m depth, and dissolves it, creating voids up to the meter range. This
dissolution process, a long-term process, occurs on the 10,000-100,000 year time scale.

435 The voids developing in the chalk start to migrate upwards through roof breakdown, once they reach a certain size. However,
thin glacial till layers in the south, mechanically stronger than the peri-glacial sand, stabilises the situation, as the entire void
and collapsed roof part is located in the saturated zone, thus buoyancy supports the strength of the thin glacial till layers in the
southern part. This situation is meta-stable, as long as there are no significant changes in groundwater level.

A drop in groundwater level, which can be initiated through pumping in the nearly open-pit mines, removes the buoyant
440 support to the glacial till above a void, and the weight of the overburden becomes too much and triggers a collapse, which
results in a sinkhole in the overlying peri-glacial sand.

8 Conclusions

The collapse sinkhole cluster on the sports field of Münsterdorf started in 2004, with an occurrence rate of about one per year. The sinkholes, typical cover-collapse sinkholes, are usually 2-3 m in diameter and 3-5 m deep. We have investigated the mechanical stability of collapse sinkholes with similar dimensions with a discrete-element model to simulate the stability conditions of the final collapse.

In the introduction, we posed three main questions, which we want to answer in this last part:

(i) **Sudden onset:**

The sudden onset of collapse sinkhole formation in 2004 points to a change in a boundary condition close to the site, e.g. changes in the mechanical and/or hydrological situation. We are able to explain the sinkhole collapse with a drop in groundwater table, reducing the buoyant force, which stabilises the existing sub-surface voids.

(ii) **Mechanical failure:**

Our mechanical models of a void in the sub-surface, embedded in the typical setup of the locality (peri-glacial sand, glacial till, and soluble chalk in 20 m depth), indicate stability of the layers above an existing sub-surface void, when the groundwater table is high.

A drop in groundwater reduces the buoyant force, which counteracts the gravitational force of the overburden, and the overburden can exceed its mechanical threshold and collapse into the void below, creating a cover-collapse sinkhole.

(iii) **Void origin:**

We have speculated about a void origin either shallow in the peri-glacial sand (6-9 m depth) of deeper in the chalk (20-22 m depth). We have shown that the shallow void might be detectable by gravity measurements, but a deeper void is not really detectable with geophysical measurements.

The high electrical conductivity, together with an elevated hydraulic permeability, which we measured with direct push-based methods in about 22.7-25 m depth, point to dissolution on top of the chalk layer, thus pointing to void spaces developing in around or below 20 m depth.

Author contributions. GK designed the setup of the numerical experiments and participated in writing the manuscript. DR designed and ran the distinct-element model runs and participated in writing the manuscript. UW performed the direct-push based measurements and participated in writing the manuscript. TV performed the direct-push based measurements and participated in writing the manuscript.

Competing interests. The authors declare that they have no competing interests.

Acknowledgements. We acknowledge funding from the BMBF within the SIMULTAN project under research grants 03G0843G (GK,DR)
470 and 03G0843F (UW,TV). Figures were prepared using GMT software (Wessel and Smith, 1998; Wessel et al., 2013) and the PARAVIEW
software (Ahrens et al., 2005; Ayachit, 2015).

References

Ahrens, J., Geveci, B., and Law, C.: Visualisation Handbook, chap. ParaView: An End-User Tool for Large Data Visualization, pp. 717–731, Elsevier, ISBN-13: 978-0123875822, 2005.

475 Atekwana, E., Atekwana, E., Rowe, R., Werkema Jr., D., and Legall, F.: The relationship of total dissolved solids measurements to bulk electrical conductivity in an aquifer contaminated with hydrocarbon, J. Applied Geophys., 56, 281–294, https://doi.org/10.1016/j.jappgeo.2004.08.003, 2004.

Ayachit, U.: The ParaView Guide: A Parallel Visualization Application, Kitware, 2015.

Blakely, R., Cruikshank, K., Johnson, A., Beeson, M., Walsh, K., and Wells, R.: A gravity study through the Tualatin Mountains, Oregon:
480 Understanding crustal structure and earthquake hazards in the Portland urban area, Tech. rep., USGS, 2010.

Bowles, J.: Foundation analysis and design, McGrw-Hill, fifth edition edn., 1997.

Buhmann, D. and Dreybrodt, W.: The kinetics of calcite dissolution and precipitation in geologically relevant situations of karst areas. 1. Open system, Chem. Geol., 48, 189–211, 1985a.

Buhmann, D. and Dreybrodt, W.: The kinetics of calcite dissolution and precipitation in geologically relevant situations of karst areas. 2.
485 Closed system, Chem. Geol., 53, 109–124, 1985b.

Christy, C. D., Christy, T. M., and Wittig, V.: A Percussion Probing Tool for the Direct Sensing of Soil Conductivity, Technical Paper 94-100, Geoprobe Systems, 1994.

Cundall, P. A. and Strack, O. D. L.: A discrete numerical model for granular assemblies, Géotechnique, 29, 47–65, https://doi.org/10.1680/geot.1979.29.1.47, 1979.

490 De Waele, J., Gutierrez, F., Parise, M., and Plan, L.: Geomorphology and natural hazards in karst areas: a review, Geomorphology, 134 (1-2), 1–8, 2011.

DIN Deutsches Institut für Normung e.V.: Geotechnische Bemessung. Normen-Handbuch Eurocode 7, vol. Band 2: Erkundung und Untersuchung DI, Beuth-Verlag, 2011.

Gebregziabher-Gared, B.: Environmental and Engineering Geophysical Studies for Sinkhole Problems Using Seismic Reflection, Refraction
495 Tomography, Electrical Resistivity Imaging, and Joint Inversions, Ph.D. thesis, Gottfried Wilhelm Leibniz Universität Hannover, 2010.

Göthling, S., Henrich, V., Klein, E., Kling, C., Muhrbeck, M., Schiperski, F., Tsami, S., and Wilke, H.: Interdisziplinäre Projektanalyse im Kreide-Tagebau bei Lägerdorf, Report, TU Berlin, 2010.

Grube, A. and Rickert, B.: Karstification of the Elmshorn salt diapir (SW Schleswig-Holstein, Germany), Z. Dt. Ges. Geowiss., 169, 547–566, 2019.

500 Grube, A., Grube, F., Rickert, B., and Strahl, J.: Eemian fossil caves and other karst structures in Cretaceous chalk and succeeding Quaternary sediments covering the salt structure Krempe-Lägerdorf (SW Schleswig-Holstein, North Germany), Z. Dt. Ges. Geowiss., 168, 263–284, 2017.

Grube, F.: Tektonische Untersuchungen in der Oberkreide von Laegerdorf (Holstein), Mitteilungen aus dem Mineralogisch-Geologischen Institut in Hamburg, 24, pp. 32, 1955.

505 Gutiérrez, F., Guerrero, J., and Lucha, P.: A genetic classification of sinkholes illustrated from evaporite paleokarst exposures in Spain, Env. Geol., 53, 993–1006, 2008a.

Gutiérrez, F., Johnsson, K. S., and Cooper, H. J.: Evaporite karst processes, landforms, and environmental problems, Env. Geol., 53, 935–936, 2008b.

Harland, M.: Radiomagnetotellurische Messungen zur Erdfallgefährdung in Münsterdorfnsterdorf (Kreis Steinburg, Schleswig-Holstein),
510   Master's thesis, Universität zu Köln, 2010.

Iwanoff, A.: Environmental impacts of deep opencast limestone mines in Lägerdorf, Northern Germany, Mine Water and the Environment,
17, 52–61, 1998.

Kaufmann, G.: Geophysical mapping of solution and collapse sinkholes, J. Appl. Geophys., 111, 271–288, 2014.

Kaufmann, G. and Romanov, D.: Structure and evolution of collapse sinkholes; Combined interpretation from physico-chemical modelling
515   and geophysical field work, J. Hydrol., 540, 688–698, https://doi.org/10.1016/j.jhydrol.2016.06.050, 2016.

Kaufmann, G., Romanov, D., Tippelt, T., Vienken, T., Werban, U., Dietrich, P., Mai, F., and Börner, F.: Mapping and modelling of collapse
sinkholes in soluble rock: the Münsterdorf site, northern Germany., J. Appl. Geophys., 154, 64–80, 2018.

Kirsch, R., ed.: Groundwater Geophysics: A Tool for Hydrogeology, Springer, 2nd edition edn., 2009.

Kirsch, R. and Werner, G.: Ergebnisse der Bohrarbeiten und Rammkernsondierungen auf dem Erdfallgelände Münsterdorf, November-
520   Dezember 2007, 2008.

Kirsch, R., Wiederhold, H., Siemon, B., Harland, M., and Gebregziabher, B.: Geophysikalische Erkundung im Erdfallgebiet Münsterdorf,
Report TK 2023/2123, LIAG & LLUR, 2011.

Kjekstad, O., Lunne, T., and Clausen, J.: Comparison between in situ cone resistance and laboratory strength for overconsolidated north sea
clays, Mar. Geotech., 3, 23–36, https://doi.org/10.1080/10641197809379792, 1978.

525   Köstler, A. and Ehrmann, W.: Fault patterns in the calcareous overburden of a salt diapir: Laegerdorf, NW Germany, N. Jb. Geol. Paläont.
Mh., H9, 555–569, 1986.

Lloyd, J.W.; Heathcote, J.: Natural Inorganic Hydrochemistry in Relation to Groundwater, Clarendon Press, Oxford, England, 1985.

Loke, M.: RES2DMOD ver. 3.03 Rapid 2D resistivity and I.P. forward modeling using the finite-difference and finite-element methods, Tech.
rep., Geotomosoft Solutions, Malaysia, 2016.

530   Loke, M. and Barker, R.: Rapid least-squares inversion of apparent resistivity pseudosections using a quasi-Newton method, Geophys.
Prospect., 44 (1), 131–152, 1995.

Loke, M. H. and Barker, R. D.: Practical techniques for 3D resistivity surveys and data inversion:, Geophysical Prospecting, 44, 499–523,
1996.

Lollino, P., Martimucci, V., and Parise, M.: Geological survey and numerical modeling of the potential failure mechanisms of underground
535   caves, Geosystem Engineering, 16 (1), 100–112, 2013.

Lunne, T. and Kleven, A.: Role of CPT in North Sea Foundation Engineering, pp. 49–75, Symposium on Cone Penetration Engineering
Division, ASCE, 1981.

Lunne, T., Robertson, R., and Powell, J.: Cone Penetration Testing in Geotechnical Practice, CRC Press, 1997.

Mai, F., Kirsch, R., Rücker, C., and Börner, F.: Petrophysical effects during karstification, in: Geophysical Research Abstracts, vol. 19, 2017.

540   McCall, W.: Application of the Geoprobe® HPT Logging System for Geo-Environmental Investigation, Tech. rep., Technical Bulletin No.
MK3184, 2011.

Messerklinger, S.: Formation mechanism of large subsidence sinkholes in the Lar valley in Iran, Quat. J. Eng. Geol. and Hydrogeol., 47,
237–250, 2014.

Olsen, C., Christensen, H., and Fabricius, I.: Static and dynamic Young's moduli of chalk from the North Sea, Geophysics, 73, E41–E50,
545   2008.

Panno, S., Kelly, W., Angel, J., and Luman, D.: Hydrogeologic and topographic controls on evolution of karst features in Illinous' sinkhole plain, Carbonates Evaporates, 28, 13–21, 2013.

Parise, M. and Gunn, J.: Natural and anthropogenic hazards in karst areas: Recognition, Analysis and Mitigation, Special Publications 279, Geological Society, London, 2007.

550 Parise, M. and Lollino, P.: A preliminary analysis of failure mechanisms in karst and man-made underground caves in Southern Italy, Geomorphology, 134 (1-2), 132–143, 2011.

Reddy, J. N.: Theory and analysis of elastic plates and shells, CRC Press, Taylor and Francis., 2007.

Robertson, P.: Cone penetration test (CPT)-based soil behaviour type (SBT) classification system - an update, Can. Geotech. J., 53, 1910–1927, https://doi.org/https://doi.org/10.1139/cgj-2016-0044, 2016.

555 Rogiers, B., Vienken, T., Gedeon, M., Batelaan, O., Mallants, D., Huysmans, M., and Dassargues, A.: Multi-scale aquifer characterization and groundwater flow model parameterization using direct push technologies, Environmental Earth Sciences, 72, 1303–1324, 2014.

Romanov, D., Kaufmann, G., and Al-Halbouni, D.: Basic processes and factors determining the evolution of collapse sinkholes - a sensitivity study, Engineering Geology, 270, https://doi.org/https://doi.org/10.1016/j.enggeo.2020.105589, 2019.

Scholtés, L. and Donzè, F.: Modelling progressive failure in fractured rock masses using a 3D discrete element method, Int. J. Rock Mech.
560 Min. Sci„ 52, 18–30, 2012.

Scholtés, L. and Donzè, F.: A DEM model for soft and hard rocks: Role of grain interlocking on strength, J. Mech. Phys. Solids, 61, 352–369, 2013.

Schulze-Dieckhoff, T.: The sinkhole area of Münsterdorf, Northern Germany - 3D GPR and ERT investigations, Master's thesis, Christian-Albrechts-Universität zu Kiel, 2015.

565 Stüwe, K.: Geodynamics of the Lithosphere: An Introduction, Springer, 1th edition edn., 2013.

Timm, R.: Seismische Untersuchungen im Erdfallgebiet Münsterdorf, Master's thesis, Christian Albrechts-Universität Kiel, 2015.

Tippelt, T., Vienken, T., Kirsch, R., Dietrich, P., and Werban, U.: Direct Push supported geotechnical and hydrogeological characterisation of an active sinkhole are, in: Geophysical Research Abstracts, vol. 19, 2017.

Topp, G., Davis, J., and Annan, P.: Electromagnetic Determination of Soil Water Content: Measurements in Coaxial Transmission Lines,
570 Water Resources Research, 16, 574–582, https://doi.org/10.1029/WR016i003p00574, 1980.

Turcotte, D. L. and Schubert, G.: Geodynamics, John Wiley and Sons, New York, 1982.

Vienken, T., Leven, C., and Dietrich, P.: Use of CPT and other direct push methods for (hydro-) stratigraphic aquifer characterization - a field study, Can. Geotech. J., 49, 197–206, 2012.

Vienken, T., Reboulet, E., Leven, C., Kreck, M., Zschornack, L., and Dietrich, P.: Field comparison of selected methods for vertical soil
575 water content profiling, Journal of Hydrology, 501, 205–212, 2013.

Šmilauer, V., Catalano, E., Chareyre, B., Dorofeenko, S., Durie, J., Dyc, N., Eliáš, J., Er, B., Eulitz, A., Gladky, A., Guo, N., Jakob, C., Kneib, F., Kozicki, J., Marzougui, D., Maurin, R., Modenese, C., Scholtès, L., Sibille, L., Stránský, J., Sweijen, T., Thoeni, K., and Yuan, C.: Yade Documentation, 2nd edition edn., 2020.

Waltham, A. and Fookes, P.: Engineering classification of karst ground conditions, Quarterly Journal of Engineering Geology and Hydroge-
580 ology, 36, 101–118, 2003.

Waltham, T., Bell, F., and Culshaw, M.: Sinkholes and Subsidence: Karst and Cavernous Rocks in Engineering and Construction, Springer, 2005.

Wessel, P. and Smith, W. H. F.: New, improved version of Generic Mapping Tools released, EOS, 79, 579, 1998.

Wessel, P., Smith, W. H. F., Scharroo, R., Luis, J. F., and Wobbe, F.: Generic Mapping Tools: Improved version released, EOS Trans. AGU,
585   94, 409–410, 2013.

Williams, P.: Encyclopedia of caves and karst science, chap. Dolines, pp. 304–310, Fitzroy Dearborn Publ. (2nd edition), 2004.
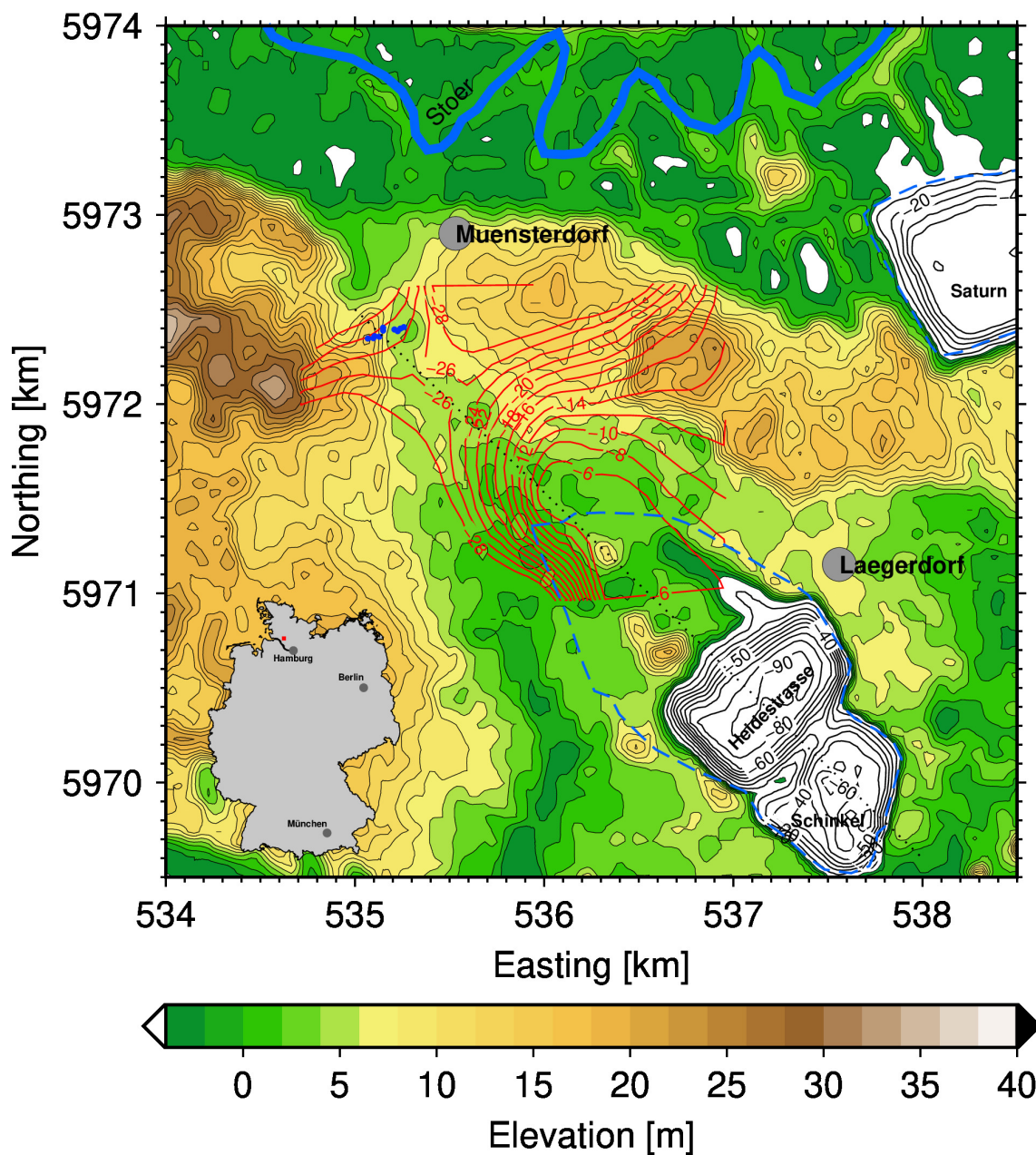
Figure 1. Topographical map of the Münsterdorf-Lägerdorf area. Shown is the elevation (colour-coded), the river Stör as local base level in the north, the villages of Münsterdorf and Lägerdorf (grey dots), the three open-pit chalk mines Saturn (abandoned), Schinkel, and Heidestrasse (black contour lines) including their actual extension (blue dashed line) not present in the SRTM model, the depth to the chalk layer (red contours), and the recent sinkholes since 2004 (blue dots). Insert: Overview map with working area marked in red.
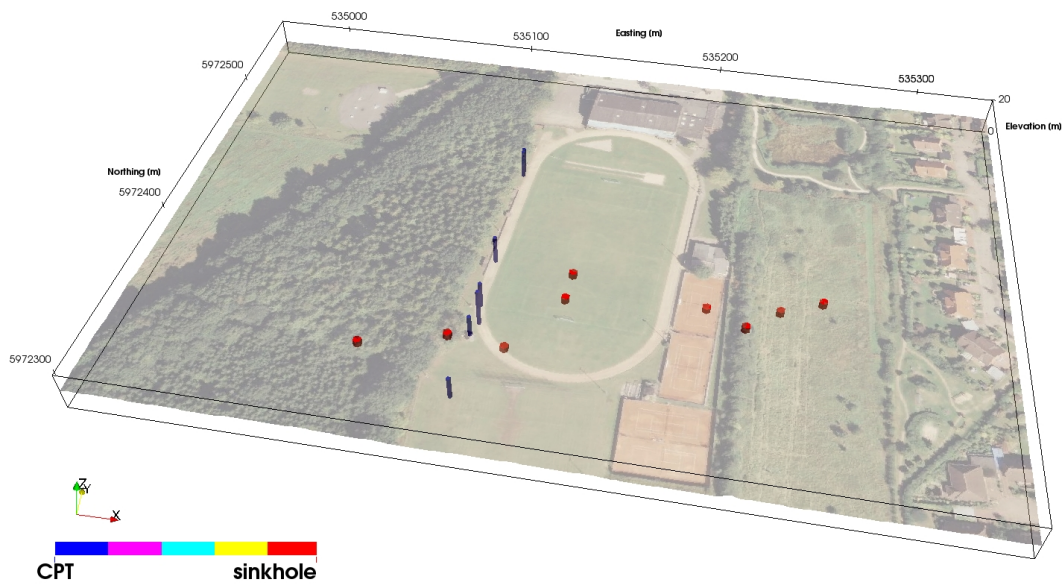
Figure 2. Sports field in Münsterdorf, view from the south towards north. Areal photo draped onto topography. The red cylinders mark the locations of the sinkholes, which occur along a narrow west-east trending line. The blue cylinders are direct push-based probe locations (shown along a south-north profile in Fig. 6). Digital orthophoto ©GeoBasis-DE/LVermGeo SH.
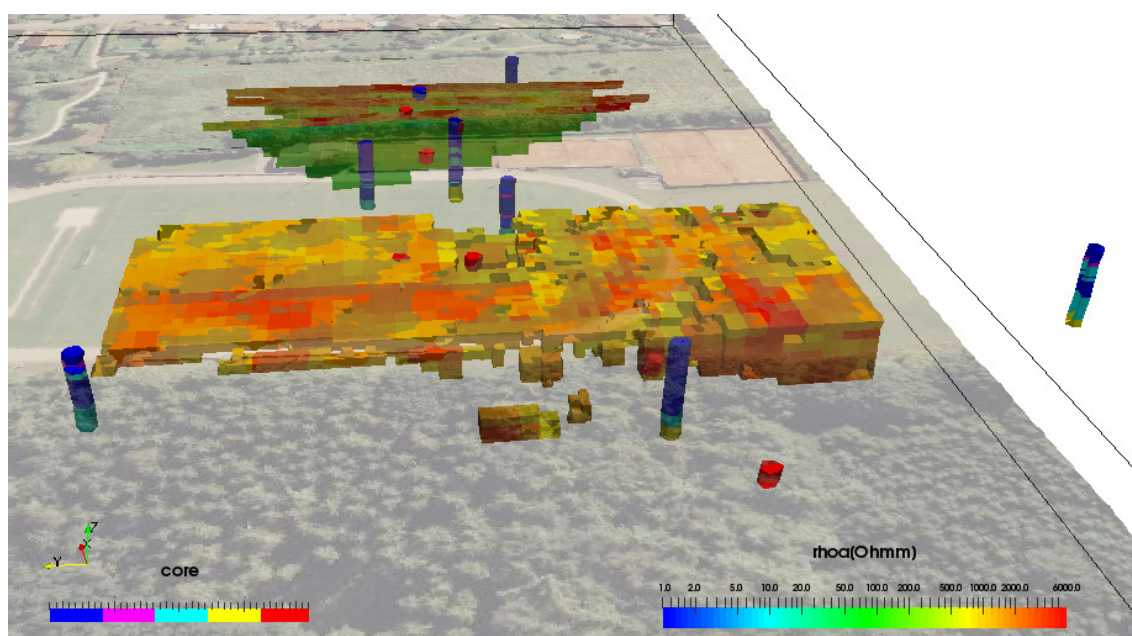
Figure 3. Sports field in Münsterdorf, view from the west towards east. The red cylinders mark the locations of the sinkholes, which occur along a narrow west-east trending line. The color-coded cylinders are boreholes from the LLUR. The blocky area underneath the sports field are mapped high electrical resistivities above 1000 Ωm from ERT profiles. In the interpretation, the anomaly delineates the dry peri-glacial sand from the more conductive glacial till. Digital orthophoto ©GeoBasis-DE/LVermGeo SH.
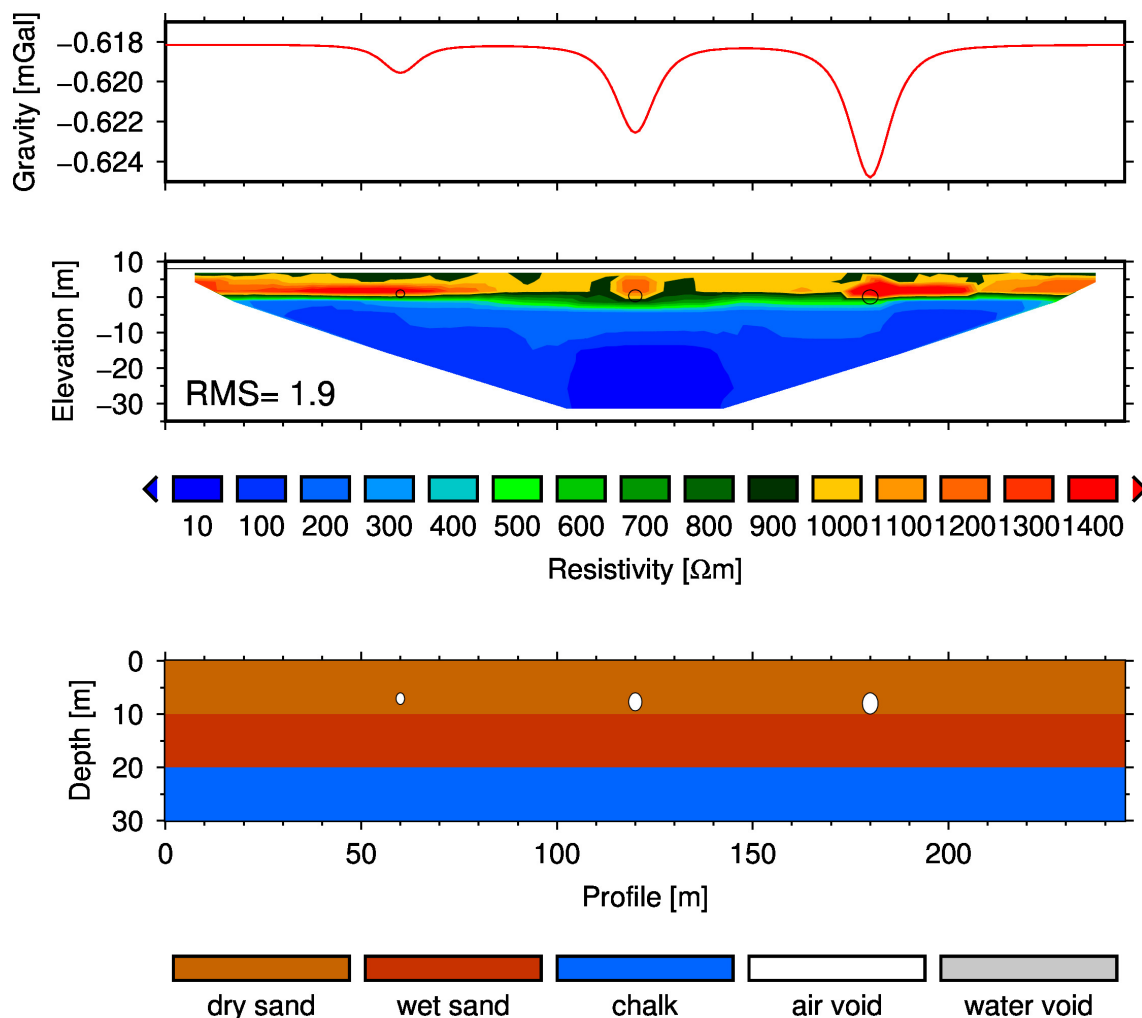
Figure 4. Prediction for Bouguer gravity (top) and electrical resistivity (middle) resulting from a given lithological structure (bottom). The structural model (bottom) comprises dry and wet peri-glacial sand (brown and red), chalk (blue), and either air-filled (white) or water-filled (gray) voids. For the first hypothesis, we located air-filled voids in around 6 m depth with radii (from left to right) of 1.1, 1.7, and 2.0 m. Density and electrical resistivity values can be found in table 1). Gravity predictions are based on a box geometry model, electrical resistivity predictions on a Wenner setup with 5 m electrode spacing.
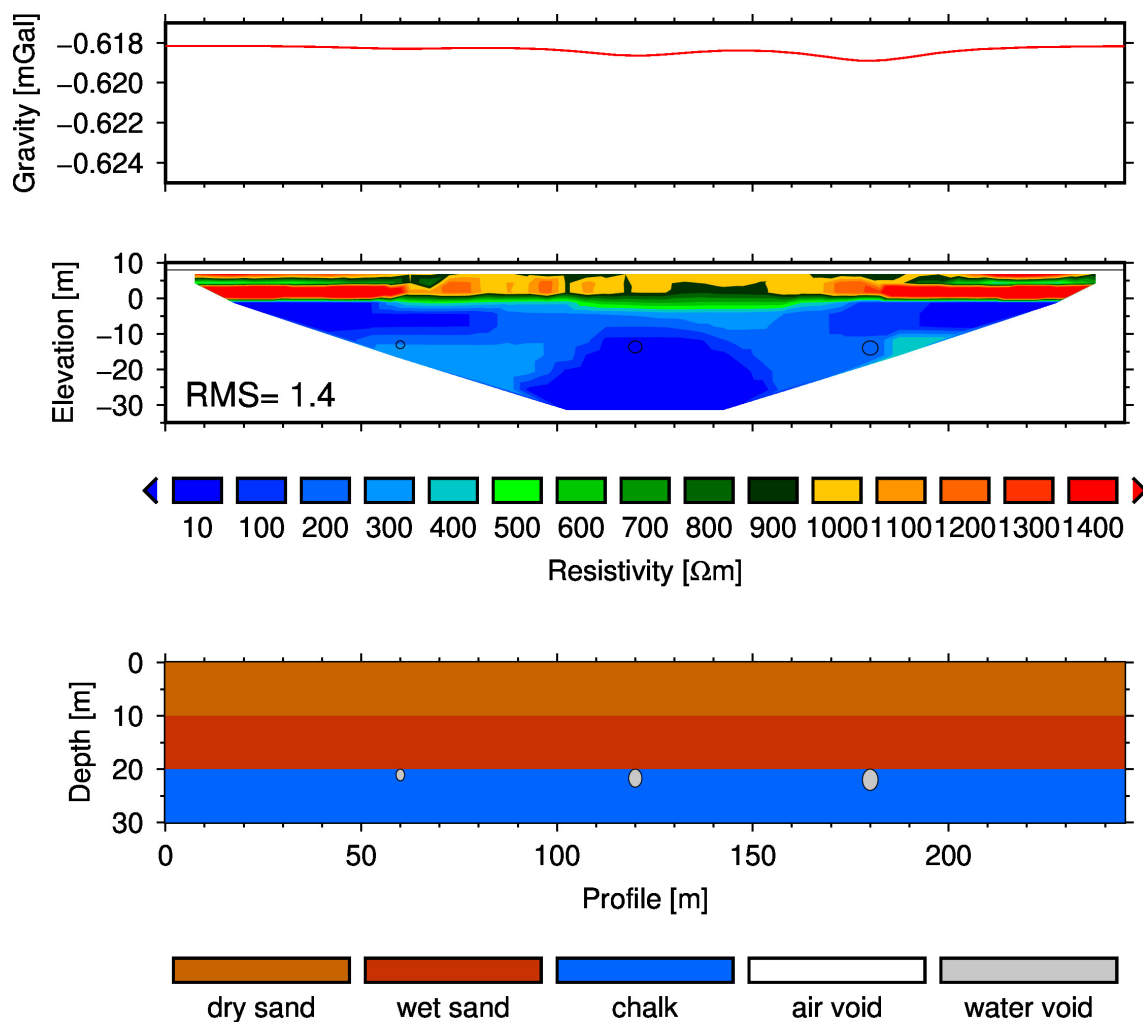
Figure 5. As Fig. 4, but voids are water filled (1000 kg/m^3 and 0.5 Ωm) and start in 20 m depth.
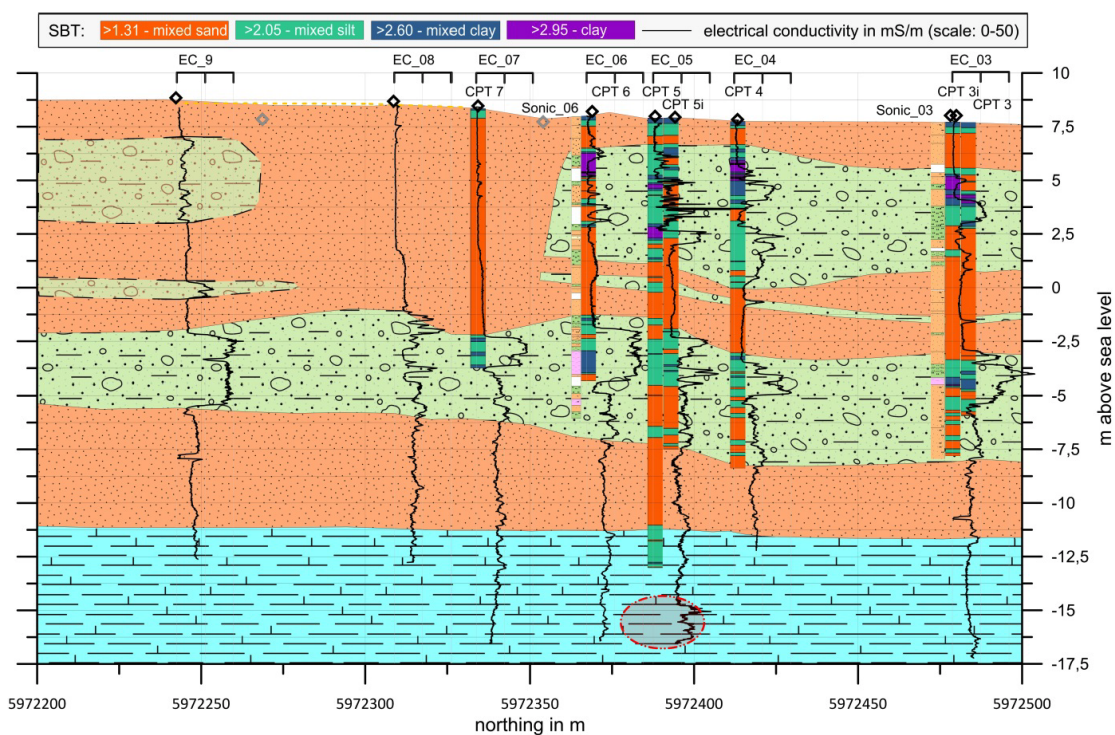
Figure 6. Results from from direct push-based methods, plotted along a a south-north transect. Direct push-based locations are labeled on top (EC_x,CPT_x, with x the core number). Borehole transects show the calculated soil-behaviour type (SBT, legend on top), and additionally electrical conductivity (EC, solid lines). The colours in the background represent the structural model interpolated from the direct push-based results (orange:peri-glacial sand, green:glacial till, blue: chalk).
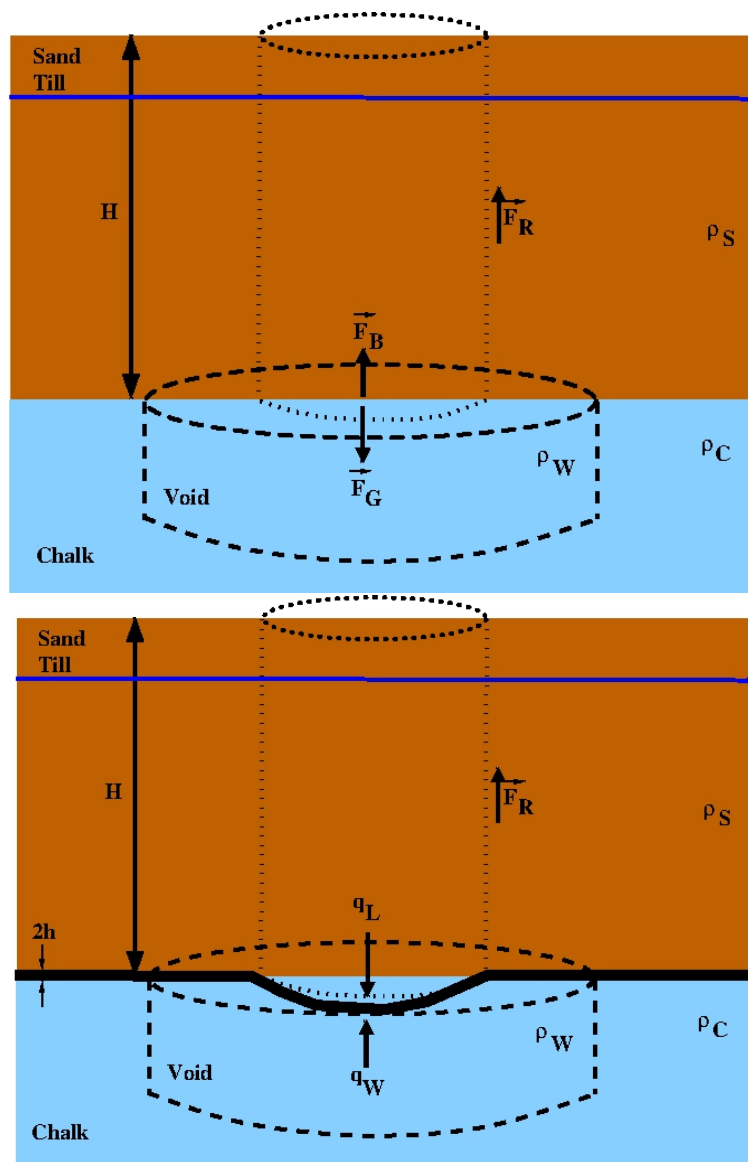
Figure 7. Simple mechanical sinkhole setup. Top: Buoyancy-driven sinkhole, void as thick dashed line, sediment pile on top as thin dotted line, forces as black arrows, water table as blue line. H is the sediment thickness. Bottom: Flexure-driven sinkhole, parameter values as above, $2h$ is the thickness of the elastic plate.
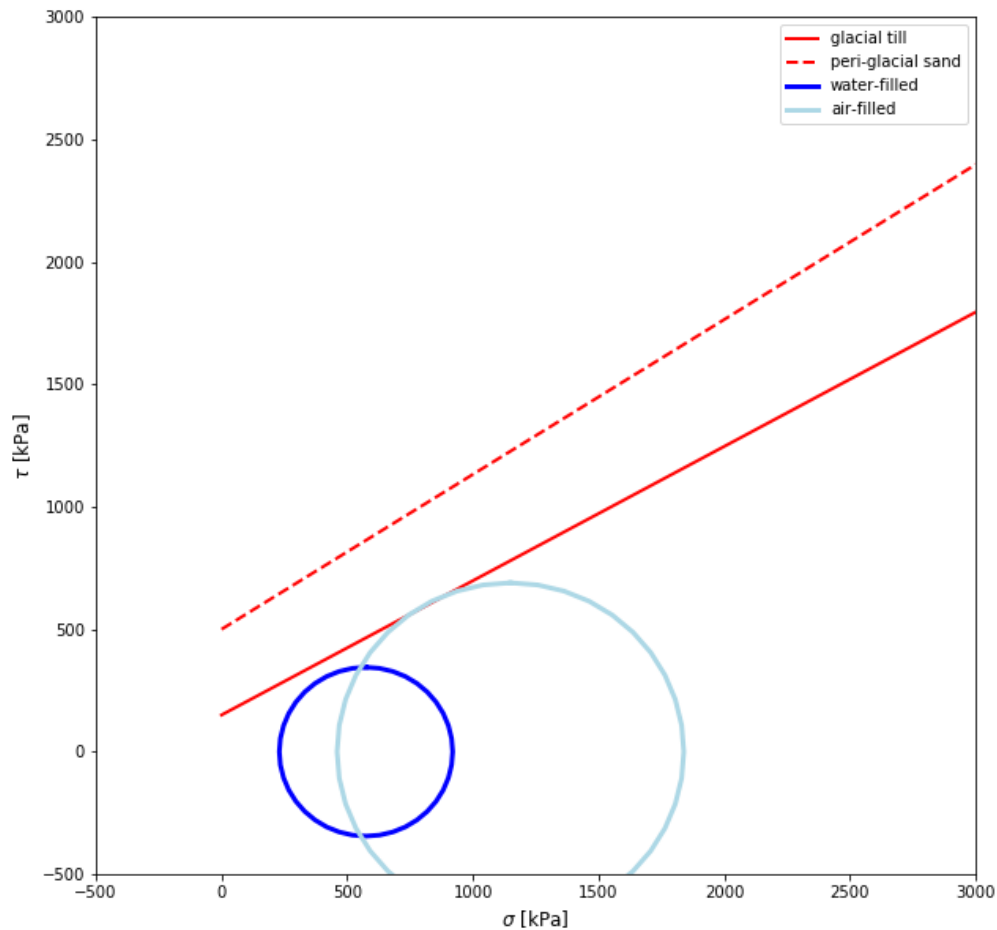
Figure 8. Mohr-Coulomb circle for stresses induced by column resting on elastic plate, with buoyancy (dark blue) and without buoyancy (light blue). The line of failure is shown for the weaker glacial till (solid red) and the stronger peri-glacial sand (dashed red), with parameter values derived from results of the direct push-based methods.
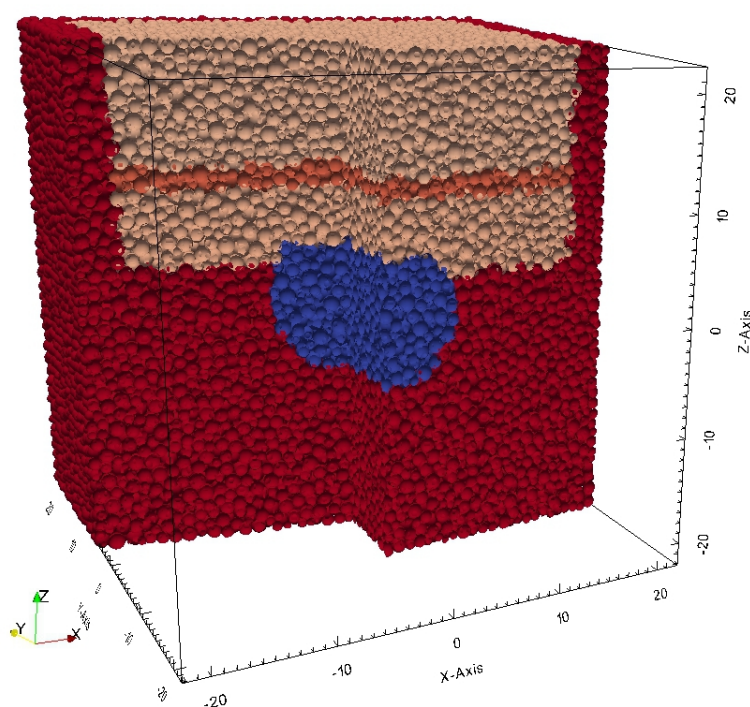
Figure 9. Setup of YADE mechanical model. The model is 50c50x50 m in size and filled with spheres irregularly packed. The colors of the sphere represent different layers: Upper peri-glacial sand (light brown), glacial till (orange), lower peri-glacial sand (light brown), chalk (red). Note that the sides of the modelling domain (also shown in red) are fixed.
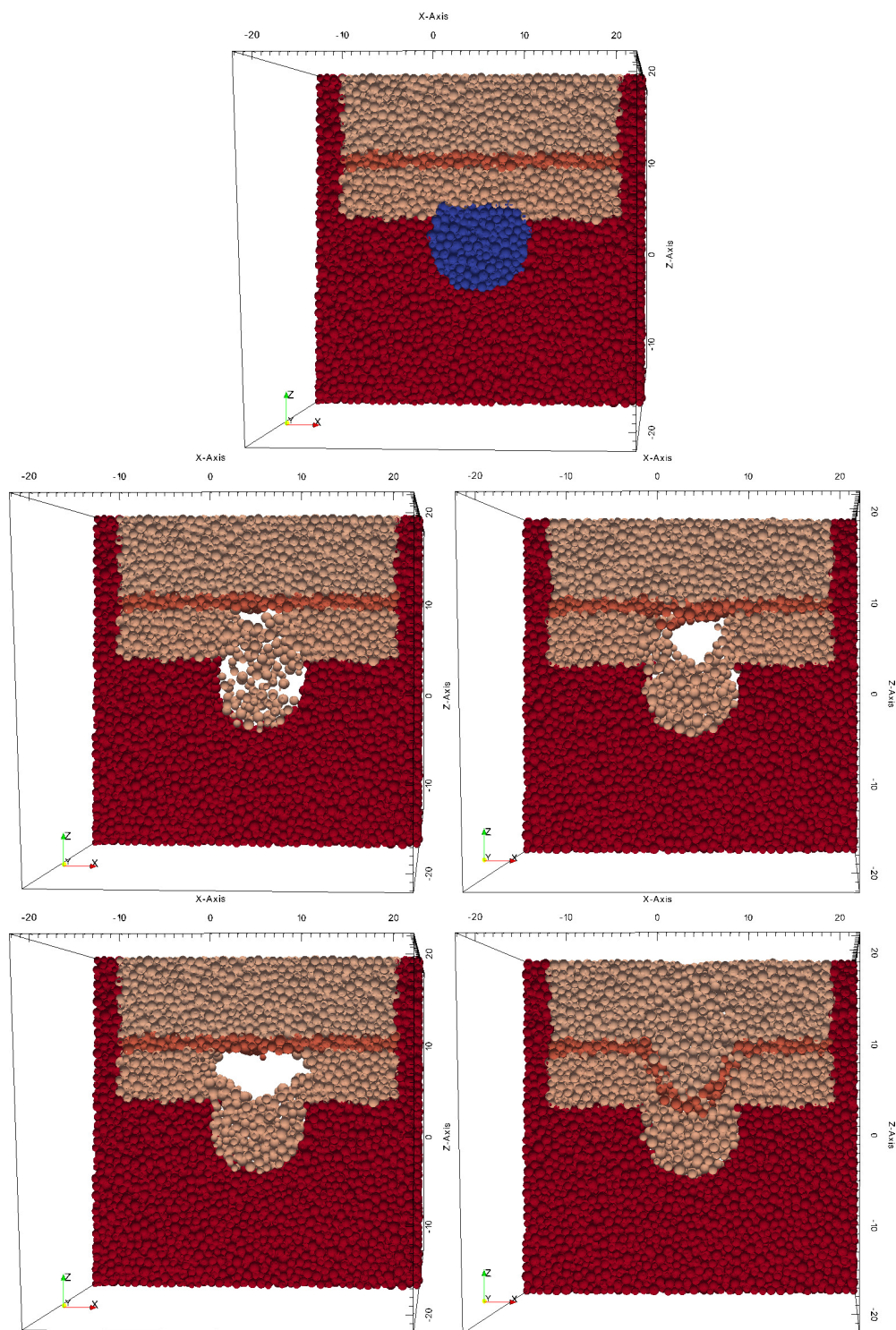
Figure 10. Mechanical breakdown simulated with YADE. Top: Initial condition, the dissolved void in the chalk is shown in blue. Left row: Two snapshots of collapse with full buoyant support. Right row: Two snapshots of collapse with partial buoyant support. Note that we show a thin slice of the 3D model, crossing the void in the chalk.
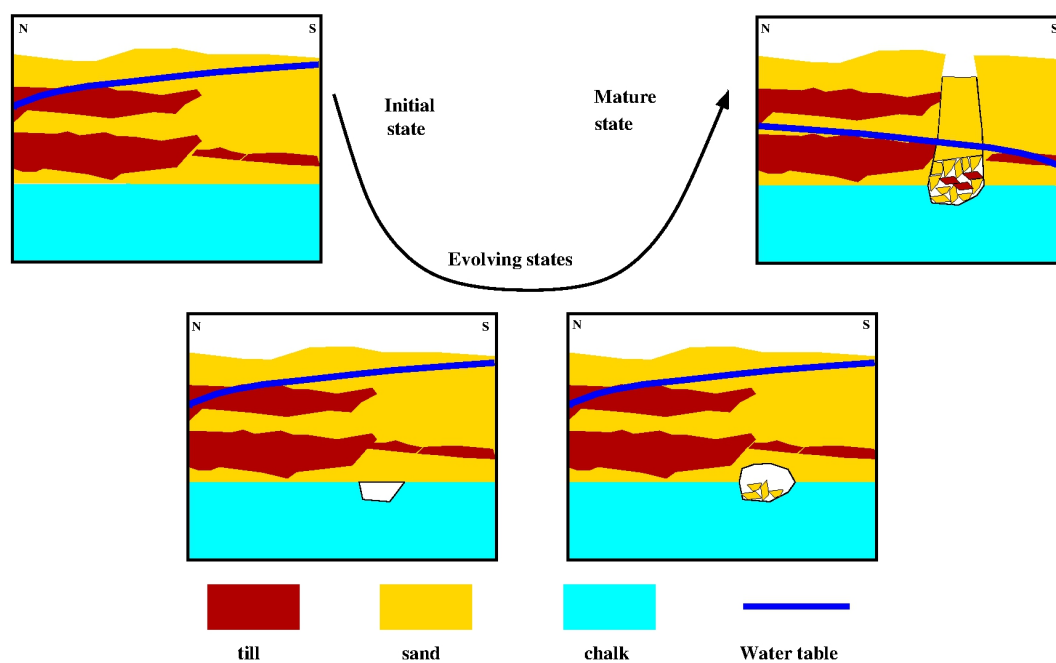
Figure 11. Evolution of collapse sinkhole. Light blue colours indicate chalk as soluble rock, yellow colours peri-glacial sand and brownish colours glacial till, the latter two as insoluble rocks. The dark blue line is the hypothetical water table, and the white area a void in the chalk.

Table 1. Material properties for different lithological layers beneath the Münsterdorf sports field. Density and electrical resistivity from Kaufmann et al. (2018). Young modulus and Poisson ratio from Bowles (1997) (sand and till) and Olsen et al. (2008) (chalk).

Material	dry sand	wet sand	glacial till	chalk	air-filled void	water-filled void
Density ρ [kg/m^3]	1800	1900	2100	2600	1.2	1000
El. resistivity ρ_e [Ωm]	1000	200-300	5-200	100-700	∞	10
Young modulus E [MPa]	10-25	50-81	10-700			
Poisson ratio ν [-]	0.3-0.4	0.4-0.4	0.2-0.5			
Friction angle α_f [°]	40-42	40-42	37			
Shear strength u_c [Pa]	300	500-600	70-150			